

Local chiral potentials and the structure of light nuclei

M. Piarulli^a, L. Girlanda^{b,c}, R. Schiavilla^{d,e}, A. Kievsky^f,
A. Lovato^a, L.E. Marcucci^{g,f}, Steven C. Pieper^a,
M. Viviani^f, and R.B. Wiringa^a

^a*Physics Division, Argonne National Laboratory, Argonne, Illinois 60439, USA*

^b*Department of Mathematics and Physics, University of Salento, 73100 Lecce, Italy*

^c*INFN-Lecce, 73100 Lecce, Italy*

^d*Theory Center, Jefferson Lab, Newport News, VA 23606, USA*

^e*Department of Physics, Old Dominion University, Norfolk, VA 23529, USA*

^f*INFN-Pisa, 56127 Pisa, Italy*

^g*Department of Physics, University of Pisa, 56127 Pisa, Italy*

(Dated: June 22, 2016)

Abstract

We present fully local versions of the minimally non-local nucleon-nucleon potentials constructed in a previous paper [M. Piarulli *et al.*, Phys. Rev. C **91**, 024003 (2015)], and use them in hyperspherical-harmonics and quantum Monte Carlo calculations of ground and excited states of ^3H , ^3He , ^4He , ^6He , and ^6Li nuclei. The long-range part of these local potentials includes one- and two-pion exchange contributions without and with Δ -isobars in the intermediate states up to order Q^3 (Q denotes generically the low momentum scale) in the chiral expansion, while the short-range part consists of contact interactions up to order Q^4 . The low-energy constants multiplying these contact interactions are fitted to the 2013 Granada database in two different ranges of laboratory energies, either 0–125 MeV or 0–200 MeV, and to the deuteron binding energy and nn singlet scattering length. Fits to these data are performed for three models characterized by long- and short-range cutoffs, R_L and R_S respectively, ranging from $(R_L, R_S) = (1.2, 0.8)$ fm down to $(0.8, 0.6)$ fm. The long-range (short-range) cutoff regularizes the one- and two-pion exchange (contact) part of the potential.

PACS numbers: 21.30.-x, 21.45.-v

I. INTRODUCTION

The understanding of the structure and reactions of nuclei and nuclear matter has been a long-standing goal of nuclear physics. In this respect, few- and many-body systems provide a laboratory for studying nuclear forces with a variety of numerical and computational techniques. In recent years, rapid advances in *ab initio* few- and many-body methods, such as no-core shell model (NCSM) [1, 2], coupled cluster (CC) [3, 4] and hyperspherical harmonics (HH) [5–8] expansions, similarity renormalization group (SRG) approaches [9, 10], self-consistent Green’s function techniques [11, 12], and quantum Monte Carlo (QMC) methods [13], in combination with the rapid increase in computational resources, have made it possible to test conventional theories and new ones, such as chiral effective field theory (χ EFT), in calculations of nuclear structure and reactions.

During the last quarter century, χ EFT, originally proposed by Weinberg in the early 1990’s [14], has been widely used for the derivation of nuclear forces and electroweak currents. Such a theory provides the most general scheme accommodating all possible interactions among nucleons, Δ isobars, and pions compatible with the relevant symmetries—in particular chiral symmetry—of low-energy quantum chromodynamics (QCD), the underlying theory of strong interactions. By its own nature, χ EFT is organized within a given power counting scheme and the resulting chiral potentials (and currents) are systematically expanded in powers of Q/Λ_χ with $Q \ll \Lambda_\chi$, where Q denotes generically a low momentum and $\Lambda_\chi \sim 1$ GeV specifies the chiral-symmetry breaking scale (see Refs. [15, 16] for recent review articles).

The power counting of χ EFT indicates that nuclear forces are dominated by nucleon-nucleon (NN) interactions, a feature which was already known before χ EFT was introduced but could be justified more formally with the advent of such a theory [14]. Many-body forces are suppressed by powers of Q ; however, the inclusion of three-nucleon forces ($3N$) is mandatory at the level of accuracy now reached by few- and many-body calculations (see [17, 18] and references therein for a comprehensive review on this topic). Being the dominant contribution of the nuclear forces, a great deal of attention has been devoted to the derivation and optimization of NN interactions.

About a decade ago, NN interactions up to next-to-next-to-next-to-leading order (N³LO or Q^4) in the chiral expansion were derived [19–28] and quantitative NN potentials were

developed [29, 30] at that order. These N3LO NN interactions are separated into pion-exchange contributions and contact terms. Pion-exchange contributions represent the long-range part of the NN interactions and include at leading order (LO or Q^0) the well-known static one-pion-exchange (OPE) potential and at higher orders, namely next-to-leading (NLO or Q^2), next-to-next-to-leading (N2LO or Q^3) and N3LO, the two-pion-exchange (TPE) potential due to leading and sub-leading πN couplings. These sub-leading chiral constants can consistently be obtained from low-energy πN scattering data [28, 31, 32]. Also three-pion-exchange (3π) shows up for the first time at N3LO; in Refs. [21, 22], it was demonstrated that the 3π contributions at this order are negligible. More recently two- and three-pion exchange contributions that occur at N4LO (Q^5) [33, 34] and N5LO (Q^6) [35] have been investigated.

Contact terms encode the short-range physics, and their strength is specified by unknown low-energy constants (LECs). In order to fix these LECs, NN chiral potentials have been confronted with the pp and np scattering databases up to lab energy of 300 MeV. These databases have been provided by the Nijmegen group [36, 37], the VPI/GWU group [38], and more recently the Granada group [39]. In the standard optimization procedure the potentials are first constrained by fitting np and pp phase shifts, and then the fit is refined by minimizing the total χ^2 obtained from a direct comparison with the NN scattering data. Entem and Machleidt [29] used their N3LO chiral potential to fit pp and np scattering data in the Nijmegen database up to laboratory energy of 290 MeV with a total χ^2/datum of 1.28. Other available chiral potentials [30] have not been fitted to scattering data directly but rather to phase shifts obtained in the Nijmegen analysis (the recent upgrade [34] of Ref. [30] relies on this procedure, while in Refs. [33, 35] a study of peripheral phase shifts is carried out with two- and three-pion exchange contributions up to order Q^5 and Q^6 , respectively).

Recently, a different optimization strategy has been introduced by A. Ekstrom *et al.* [40]. This new approach is based on a simultaneous fit of the NN and $3N$ forces to low-energy NN data, deuteron binding energy, and binding energies and charge radii of hydrogen, helium, carbon, and oxygen isotopes. These authors considered the $NN + 3N$ interaction at N2LO, namely N2LO_{sat}, where the NN sector is constrained by pp and np scattering observables from the SM99 database up to 35 MeV scattering energy in the laboratory system with a total $\chi^2/\text{datum} \approx 4.3$.

The family of NN chiral interactions mentioned above are formulated in momentum-space and have the feature of being strongly non-local in coordinate space, making them not well-suited for certain numerical algorithms, for example QMC. Up to until recently, QMC methods, such as variational Monte Carlo (VMC), Green’s function Monte Carlo (GFMC) and auxiliary field diffusion Monte Carlo (AFDMC), have been used to compute the properties of light nuclei with mass number $A \leq 12$, closed shell nuclei ^{16}O and ^{40}Ca , and nucleon matter by using phenomenological nuclear Hamiltonians based on the Argonne v_{18} (AV18) two-nucleon potential [41] and the Urbana/Illinois (U/IL) series of three-nucleon potentials [42–45]. While QMC has had great success in predicting many nuclear properties, such as spectra, electromagnetic form factors, electroweak transitions, low-energy scattering and response, nevertheless it has been limited to realistic Hamiltonians based on the AV18 and U/IL models and other simpler local interactions. The reason is that local coordinate-space interactions are particularly convenient for QMC techniques, and the AV18 and U/IL models fall into this category, while many of the available NN chiral interactions have strong non-localities. These non-localities come about because of (i) the specific choice made to regularize the momentum space potential, and (ii) contact interactions that depend not only on the momentum transfer $\mathbf{k} = \mathbf{p}' - \mathbf{p}$ but also on $\mathbf{K} = (\mathbf{p}' + \mathbf{p})/2$ (\mathbf{p} and \mathbf{p}' are the initial and final relative momenta of the two nucleons).

Local chiral interactions were developed up to N2LO (or Q^3) [46, 47] only recently. These interactions are regularized in coordinate space by a cutoff depending only on the relative distance between the two nucleons, and use Fierz identities to remove completely the dependence on the relative momentum $-i\nabla$ (or equivalently \mathbf{K}), by selecting appropriate combinations of contact operators. The LECs multiplying these contact terms have been fixed by performing χ^2 fits to the np phase shifts from the Nijmegen partial-wave analysis (PWA) up to 150 MeV lab energy. The resulting chiral potentials have been used in GFMC calculations for $A \leq 5$ nuclei and AFDMC calculations of neutron matter [47–49]. While this Fierz re-arrangement is effective in completely removing non-localities at N2LO, it cannot do so at N3LO. As shown in Ref. [50], operator structures depending quadratically on $-i\nabla$ are unavoidable, and therefore the potentials constructed in Ref. [50] belong to the class of “minimally non-local” chiral potentials at N3LO.

In the present work we construct fully local versions of these minimally non-local NN potentials [50] by dropping the terms proportional to ∇^2 , and use them in HH, VMC and

GFMC calculations of ground and excited states of ${}^3\text{H}$, ${}^3\text{He}$, ${}^4\text{He}$, ${}^6\text{He}$, and ${}^6\text{Li}$ nuclei. The paper is organized as follows. In the next section we summarize the main points of Ref. [50], and then proceed to discuss the modifications adopted in this work in order to construct the new class of local potentials. In Sec. III we provide the χ^2 values obtained by performing different types of fits, show the calculated phase shifts for the lower partial waves (S, P, and D waves), and compare these phase shifts to those from recent PWA's. There we also provide tables of the pp , np and nn effective range parameters and deuteron properties. In Sec. IV the HH, VMC and GFMC methods are briefly described and results for the binding energies of $A = 3, 4$, and 6 nuclei are discussed. Clearly, the N3LO calculations reported here with only two-body forces are incomplete, since three-body forces start to come in at N2LO. Nevertheless, they provide the basis for the calculations of light nuclei structure based on chiral two- *and* three-body forces which will follow.

II. LOCAL CHIRAL NN POTENTIALS

Following Ref. [50], the local NN potential constructed in the present work is written as a sum of an electromagnetic-interaction component, v_{12}^{EM} , and a strong-interaction component, v_{12} . The v_{12}^{EM} interaction is the same as that used in the AV18 potential [41], while the v_{12} one is obtained in χEFT and is conveniently separated into long- and short-range parts, respectively v_{12}^{L} and v_{12}^{S} . The v_{12}^{L} part includes the one-pion-exchange (OPE) and two-pion-exchange (TPE) contributions up to N2LO (or Q^3) in the chiral expansion. The TPE component also contains diagrams involving Δ -isobars in intermediate states [50].

The strength of this long-range part is fully determined by the nucleon and nucleon-to- Δ axial coupling constants g_A and h_A , the pion decay amplitude F_π , and the sub-leading N2LO LECs c_1 , c_2 , c_3 , c_4 , and $b_3 + b_8$, constrained by reproducing πN scattering data [28]. Note that the LEC ($b_3 + b_8$) is explicitly retained in our fitting procedure, even though it has been shown to be redundant at this order [51]. Here and in what follows, we adopt the same values for pion and nucleon masses, F_π , g_A and h_A and the sub-leading N2LO LECs as listed in Tables I and II of Ref. [50].

The potential v_{12}^{L} can be written in coordinate space as a sum of 8 operators,

$$v_{12}^{\text{L}} = \left[\sum_{l=1}^6 v_{\text{L}}^l(r) O_{12}^l \right] + v_{\text{L}}^{\sigma T}(r) O_{12}^{\sigma T} + v_{\text{L}}^{tT}(r) O_{12}^{tT} , \quad (1)$$

where

$$O_{12}^{l=1,\dots,6} = [\mathbf{1}, \boldsymbol{\sigma}_1 \cdot \boldsymbol{\sigma}_2, S_{12}] \otimes [\mathbf{1}, \boldsymbol{\tau}_1 \cdot \boldsymbol{\tau}_2] , \quad (2)$$

$O_{12}^{\sigma T} = \boldsymbol{\sigma}_1 \cdot \boldsymbol{\sigma}_2 T_{12}$, and $O_{12}^{tT} = S_{12} T_{12}$, and $T_{12} = 3 \tau_{1z} \tau_{2z} - \boldsymbol{\tau}_1 \cdot \boldsymbol{\tau}_2$ is the isotensor operator. The first 6 terms (the so-called v_6 operator structure) in Eq. (1) are the charge-independent (CI) central, spin, and tensor components without and with the isospin dependence $\boldsymbol{\tau}_1 \cdot \boldsymbol{\tau}_2$, while the last two terms (proportional to T_{12}) are the charge-independence breaking (CIB) central and tensor components induced by the difference between the neutral and charged pion masses in the OPE. The radial functions $v_L^l(r)$, $v_L^{\sigma T}(r)$, and $v_L^{tT}(r)$ are explicitly given in Appendix A of [50]. The singularities at the origin are regularized by cutoff functions of the form

$$C_{R_L}(r) = 1 - \frac{1}{(r/R_L)^6 e^{(r-R_L)/a_L} + 1} , \quad (3)$$

where three values for the radius R_L are considered, $R_L = (0.8, 1.0, 1.2)$ fm with the diffuseness a_L fixed at $a_L = R_L/2$ in each case.

The main difference between the potentials constructed in Ref. [50] and those in the current work lies in the operator structure of their short-range components, which we now take to have the form

$$v_{12}^S = \sum_{l=1}^{16} v_S^l(r) O_{12}^l , \quad (4)$$

where $O_{12}^{l=1,\dots,6}$ have been defined above,

$$O_{12}^{l=7,\dots,11} = \mathbf{L} \cdot \mathbf{S}, \mathbf{L} \cdot \mathbf{S} \boldsymbol{\tau}_1 \cdot \boldsymbol{\tau}_2, (\mathbf{L} \cdot \mathbf{S})^2, \mathbf{L}^2, \mathbf{L}^2 \boldsymbol{\sigma}_1 \cdot \boldsymbol{\sigma}_2 , \quad (5)$$

and

$$O_{12}^{l=12,\dots,16} = T_{12}, (\tau_1^z + \tau_2^z), \boldsymbol{\sigma}_1 \cdot \boldsymbol{\sigma}_2 T_{12}, S_{12} T_{12}, \mathbf{L} \cdot \mathbf{S} T_{12} . \quad (6)$$

The parametrization above differs in two ways from that of the minimally non-local potential of Ref. [50]. The first difference concerns the \mathbf{p}^2 terms

$$\{ v_S^p(r) + v_S^{p\sigma}(r) \boldsymbol{\sigma}_1 \cdot \boldsymbol{\sigma}_2 + v_S^{pt}(r) S_{12} + v_S^{pt\tau}(r) S_{12} \boldsymbol{\tau}_1 \cdot \boldsymbol{\tau}_2 , \mathbf{p}^2 \} ,$$

which are now absent in Eq. (4). The second difference has to do with the charge-symmetry breaking (CSB) piece of v_{12}^S , which, in contrast to Ref. [50], includes only the LO term proportional to $(\tau_1^z + \tau_2^z)$ needed to reproduce the singlet nn scattering length.

The radial functions $v_S^l(r)$ are the same as those listed in Appendix B of Ref. [50], and involve a local regulator (to replace the δ functions) taken as

$$C_{R_S}(r) = \frac{1}{\pi^{3/2} R_S^3} e^{-(r/R_S)^2}, \quad (7)$$

where we consider, in combination with $R_L = (0.8, 1.0, 1.2)$ fm, $R_S = (0.6, 0.7, 0.8)$ fm, corresponding to typical momentum-space cutoffs $\Lambda_S = 2/R_S$ ranging from about 660 MeV down to 500 MeV. Hereafter we will denote the potential with cutoffs $(R_L, R_S) = (1.2, 0.8)$ fm as model *a*, that with $(1.0, 0.7)$ fm as model *b*, and that with $(0.8, 0.6)$ fm as model *c*. These radial functions contain 26 LECs. Of these, 20 are in the charge-independent part of v_{12}^S : 2 at LO (Q^0), 7 at NLO (Q^2), and 11 at N3LO (Q^4). The remaining 6 are in its charge-dependent part: 2 at LO (one each from CIB and CSB), and 4 at NLO from CIB. The optimization procedure to fix these 26 LECs is the same as that adopted in Ref. [50], and is discussed in the next section. It uses pp and np scattering data (including normalizations), as assembled in the Granada database [39], the nn scattering length, and the deuteron binding energy. The minimization of the objective function χ^2 with respect to the LECs is carried out with the Practical Optimization Using no Derivatives (for Squares), POUNDerS [52].

III. TOTAL χ^2 AND PHASE SHIFTS

We report results for the local potentials $v_{12} + v_{12}^{\text{EM}}$ described in the previous section and corresponding to three different choices of cutoffs (R_L, R_S) : model *a* with $(1.2, 0.8)$ fm, model *b* with $(1.0, 0.7)$ fm, and model *c* with $(0.8, 0.6)$ fm. Models *a*, *b*, and *c* are fitted to the Granada database of pp and np observables in two different ranges of laboratory energies, either 0–125 MeV or 0–200 MeV, to the deuteron binding energy and nn singlet scattering length. For convenience potential models *a*, *b*, and *c* fitted up to 200 MeV laboratory energy are labelled as \tilde{a} , \tilde{b} and \tilde{c} , respectively. We list the total number of pp and np data (including normalizations) and corresponding total χ^2 per datum for all the potentials in Table I. The total number of data points, N_{pp+np} , changes slightly for each of the various models because of fluctuations in the number of normalizations (see Ref. [50] for more details on the fit procedure). For model *b* we performed fits of the Granada database up to 125 MeV order by order in the chiral expansion. The total χ^2/datum are 59.88, 2.18, 2.32 and 1.07 at LO, NLO, N2LO and N3LO, respectively. There is a strong reduction in the total χ^2 going from

model	order	E_{Lab} (MeV)	N_{pp+np}	χ^2/datum
b	LO	0–125	2558	59.88
b	NLO	0–125	2648	2.18
b	N2LO	0–125	2641	2.32
b	N3LO	0–125	2665	1.07
a	N3LO	0–125	2668	1.05
c	N3LO	0–125	2666	1.11
\tilde{a}	N3LO	0–200	3698	1.37
\tilde{b}	N3LO	0–200	3695	1.37
\tilde{c}	N3LO	0–200	3693	1.40
a	N3LO	0–200	3690	2.41
b	N3LO	0–200	3679	3.76
c	N3LO	0–200	3679	4.52

TABLE I: Total χ^2/datum for model a (\tilde{a}) with $(R_L, R_S) = (1.2, 0.8)$ fm, model b (\tilde{b}) with $(1.0, 0.7)$ fm, and model c (\tilde{c}) with $(0.8, 0.6)$ fm fitted up to 125 (200) MeV laboratory energy. For model b , results of the fits up to 125 MeV order by order in the chiral expansion are also given; N_{pp+np} denotes the total number of pp and np data, including observables and normalizations.

LO and NLO and from N2LO and N3LO. However, the quality of the fit worsens slightly in going from NLO to N2LO. At N2LO we fixed the chiral LECs, namely c_1 , c_2 , c_3 , c_4 and $b_3 + b_8$, from the πN scattering analysis of Ref. [28]. In the range 0–125 MeV, the total χ^2/datum at N3LO are 1.05, 1.07, 1.11 for models a , b , and c , respectively; while in the range 0–200 MeV the total χ^2/datum at N3LO are 1.37, 1.37, 1.40. The total χ^2/datum at N3LO for models a , b , and c when compared (without refitting) to the 0–200 MeV database are 2.41, 3.76, 4.52, respectively. In both energy ranges, the quality of the fits deteriorates slightly as the (R_L, R_S) cutoffs are reduced from the values $(1.2, 0.8)$ fm of model a down to $(0.8, 0.6)$ fm of model c .

The fitted values of the LECs corresponding to models a , b , c and \tilde{a} , \tilde{b} , \tilde{c} are listed in Tables II and III, respectively. The values for the πN LECs in the OPE and TPE terms of these models are given in Table I of Ref. [50].

The np and pp S-wave, P-wave, and D-wave phase shifts for potential models fitted up to 125 MeV and 200 MeV laboratory energy are displayed in Figs. 1 and 2, respectively. The top two panels of these figures show the phase shifts for np in $T=1$ and $T=0$ channels, respectively, while the remaining bottom panels show the pp phase shifts (in $T=1$ channel). The width of the shaded band represents the cutoff sensitivity of the phases obtained with the full models a , b , and c , including strong and electromagnetic interactions. The calculated phases are compared to those obtained in PWA's by the Nijmegen [36], Granada [39], and Gross-Stadler [53] groups. The recent Gross and Stadler's PWA is limited to np data only.

In Fig. 3, the np (top panels) and pp (lower panel) S-wave, P-wave, and D-wave phase shifts are displayed for model b up to 125 MeV lab energy order-by-order in the chiral expansion. Dashed (blue), dash-dotted (green), double-dash-dotted (magenta), and solid (red) lines represent the results at LO, NLO, N2LO and N3LO, respectively. Of course, the description of the phase shifts improves substantially, as one progresses from LO to N3LO.

The low-energy scattering parameters are listed in Table IV, where they are compared to experimental results [54–58]. The singlet and triplet np , and singlet pp and nn , scattering lengths are calculated with the inclusion of electromagnetic interactions. Without the latter, the effective range function is simply given by $F(k^2) = k \cot \delta = -1/a + r k^2/2$ up to terms linear in k^2 . In the presence of electromagnetic interactions, a more complicated effective range function must be used; it is reported in Appendix D of Ref. [50], along with the relevant references.

The static deuteron properties are shown in Table V and compared to experimental values [59–62]. The binding energy E_d is fitted exactly and includes the contributions (about 20 keV) of electromagnetic interactions, among which the largest is that due to the magnetic moment term. The asymptotic S-state normalization, A_S , deviates less than 1% from the experimental data, and the D/S ratio, η , is ~ 2 standard deviations from experiment for all models considered. The deuteron (matter) radius, r_d , is under-predicted by about 0.2–1.0%. It should be noted that this observable has negligible contributions due to two-body electromagnetic operators [63]. The magnetic moment, μ_d , and quadrupole moment, Q_d , experimental values are underestimated by all models, but these observables are known to have significant corrections from (isoscalar) two-body terms in nuclear electromagnetic charge and current operators [63]. Their inclusion would bring the calculated values considerably closer to experiment.

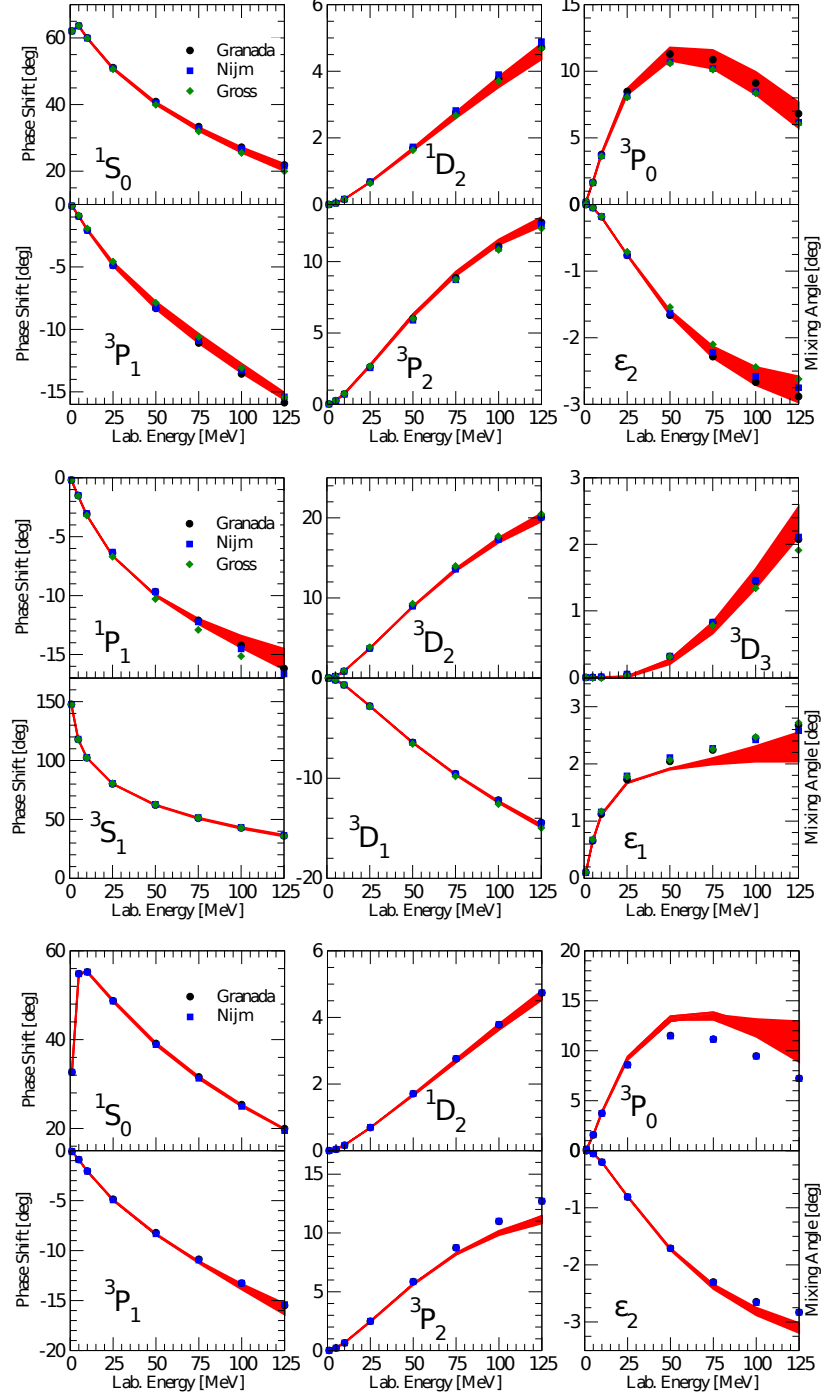


FIG. 1: (Color online) S-wave, P-wave, and D-wave phase shifts for np in $T=0$ and 1 states (top two panels) and pp (lower panel), obtained in the Nijmegen [36, 37], Gross and Stadler [53], and Granada [39] PWA's, are compared to those of models a , b , and c , indicated by the band.

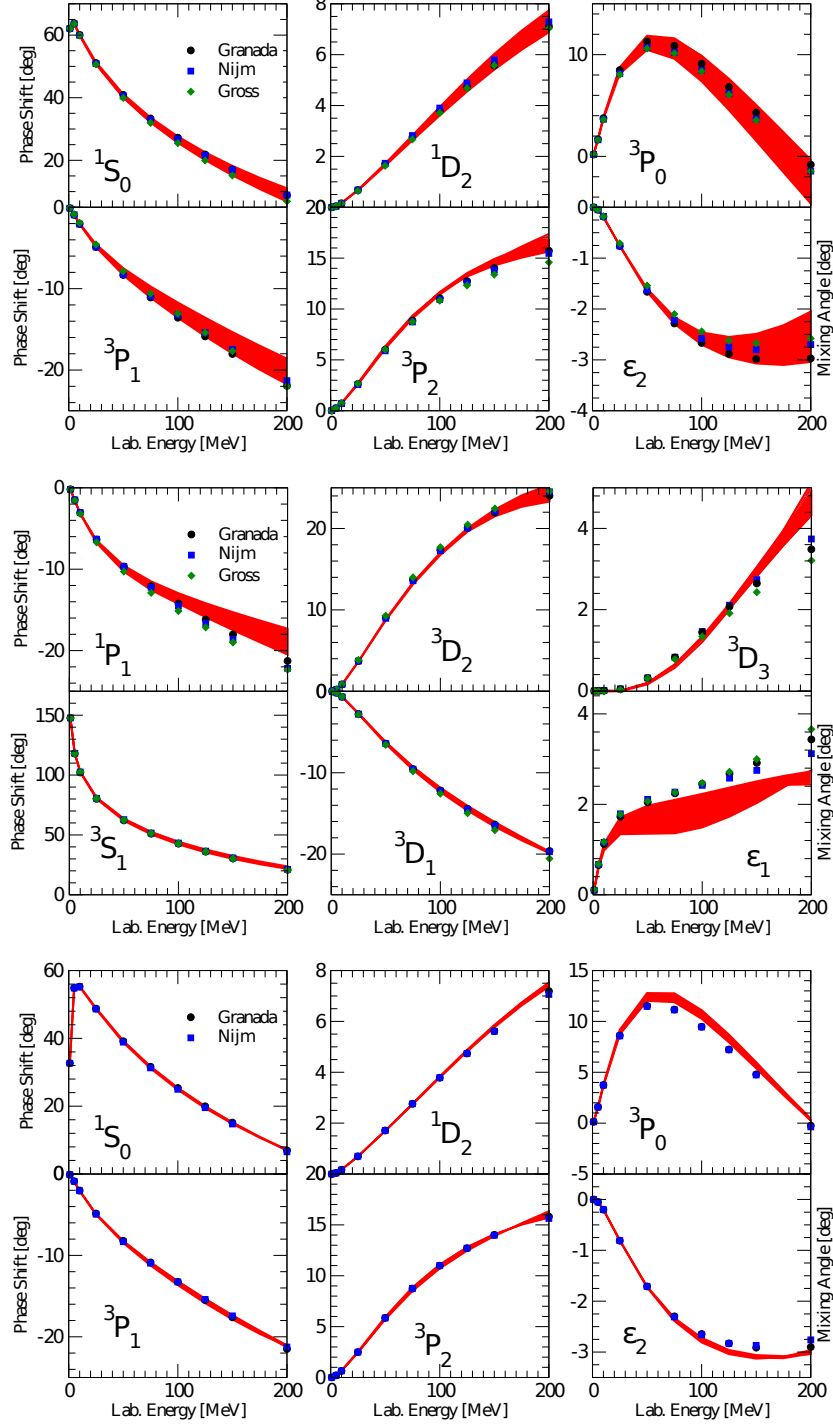


FIG. 2: (Color online) Same as Fig. 1 but for models \tilde{a} , \tilde{b} , and \tilde{c} fitted to 200 MeV lab energy.

IV. HH AND QMC CALCULATIONS FOR LIGHT NUCLEI

The study of light nuclei is especially interesting since it provides the opportunity to test, in essentially exact numerical calculations, models of two- and three-nucleon forces. In this

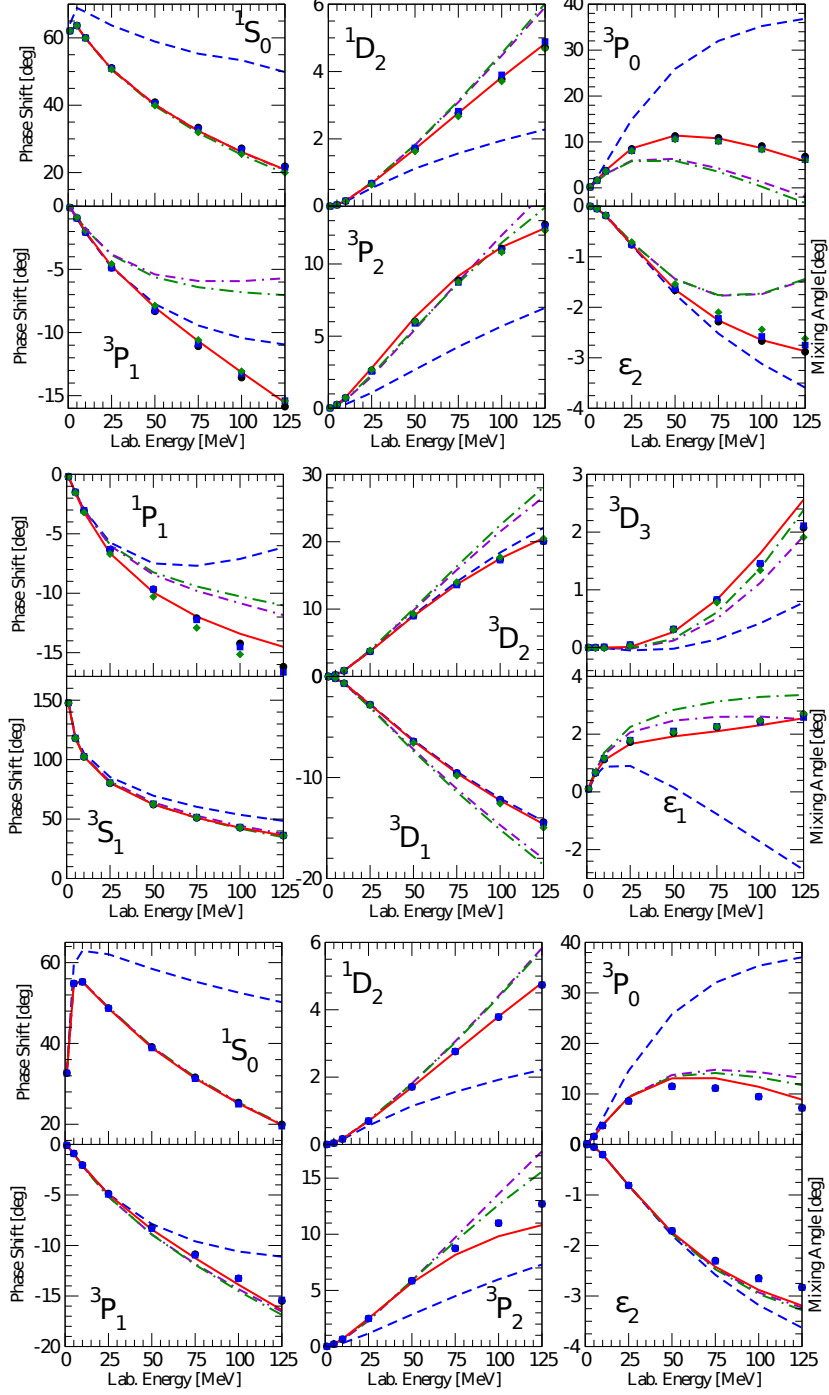


FIG. 3: (Color online) Chiral expansion of the np (top two panels) and pp (bottom panel) S-wave, P-wave, and D-wave phase shifts up to 125 MeV for model b in comparison with the Nijmegen [36, 37], Gross and Stadler [53], and Granada [39] PWA's. Dashed (blue), dash-dotted (green), double-dash-dotted (magenta), and solid (red) lines show the results at LO, NLO, N2LO and N3LO, respectively.

TABLE II: Values of the LECs corresponding to potential models a , b , c (fitted up to 125 MeV lab energy). The notation $(\pm n)$ means $\times 10^{\pm n}$.

LECs	Model a	Model b	Model c
C_S (fm ²)	0.2726141(+1)	0.8038124(+1)	0.1858356(+2)
C_T (fm ²)	-0.5228448	-0.1203741(+1)	-0.6118406(+1)
C_1 (fm ⁴)	-0.6992838(-1)	-0.2280422	-0.5624246
C_2 (fm ⁴)	-0.1496013	-0.2249889	-0.3529711
C_3 (fm ⁴)	-0.2502401(-1)	-0.4007665(-1)	-0.2225345
C_4 (fm ⁴)	-0.2728396(-1)	0.1243960(-1)	0.3381613(-1)
C_5 (fm ⁴)	-0.6530008(-2)	-0.1870727(-1)	-0.2881762(-1)
C_6 (fm ⁴)	-0.7554924(-1)	-0.7406609(-1)	-0.6535759(-1)
C_7 (fm ⁴)	-0.1017206(+1)	-0.1197452(+1)	-0.1464748(+1)
D_1 (fm ⁶)	-0.4251199(-1)	-0.3820959(-1)	-0.2163208(-1)
D_2 (fm ⁶)	-0.5567938(-2)	-0.5343034(-2)	0.2866318(-2)
D_3 (fm ⁶)	-0.1666607(-1)	-0.1601394(-1)	-0.1472287(-1)
D_4 (fm ⁶)	0.1054347(-2)	0.4219347(-2)	0.1052796(-2)
D_5 (fm ⁶)	0.5383828(-2)	0.8971752(-2)	0.7477159(-2)
D_6 (fm ⁶)	-0.8012050(-2)	-0.5986245(-2)	-0.2247046(-2)
D_7 (fm ⁶)	-0.2309392(-1)	-0.6180197(-2)	0.3616700(-1)
D_8 (fm ⁶)	0.1383136(-1)	0.1782567(-1)	0.2903320(-1)
D_9 (fm ⁶)	0.4797012(-1)	0.3094851(-1)	0.9175910(-1)
D_{10} (fm ⁶)	-0.1156876	-0.8073891(-1)	-0.1229688
D_{11} (fm ⁶)	-0.1453295(-1)	-0.1162060(-1)	-0.2671576(-1)
C_0^{IV} (fm ²)	0.9325477(-2)	0.1018989(-1)	0.1357818(-1)
C_0^{IT} (fm ²)	0.1578240(-1)	0.2416591(-1)	0.2195881(-1)
C_1^{IT} (fm ⁴)	-0.2179452(-2)	-0.3707396(-2)	-0.2698274(-2)
C_2^{IT} (fm ⁴)	-0.6288540(-2)	-0.3601899(-2)	-0.1288174(-2)
C_3^{IT} (fm ⁴)	-0.5799803(-2)	-0.4559006(-2)	-0.3126089(-3)
C_4^{IT} (fm ⁴)	0.2250167(-1)	0.1859997(-1)	0.8987538(-2)

TABLE III: Same as Table II but for potential models \tilde{a} , \tilde{b} , \tilde{c} (fitted up to 200 MeV lab energy).

LECs	Model \tilde{a}	Model \tilde{b}	Model \tilde{c}
C_S (fm ²)	0.2936041(+1)	0.8398499(+1)	0.1858331(+2)
C_T (fm ²)	-0.4933897	-0.1207696(+1)	-0.6116424(+1)
C_1 (fm ⁴)	-0.1013462	-0.2324413	-0.5565484
C_2 (fm ⁴)	-0.1444844	-0.2108143	-0.3574422
C_3 (fm ⁴)	-0.3647634(-1)	-0.3461629(-1)	-0.2266117
C_4 (fm ⁴)	-0.1630825(-1)	0.8748772(-2)	0.3921168(-1)
C_5 (fm ⁴)	-0.6658100(-2)	-0.3614304(-1)	-0.2661419(-1)
C_6 (fm ⁴)	-0.6176835(-1)	-0.5542581(-1)	-0.6532432(-1)
C_7 (fm ⁴)	-0.9578191	-0.1019849(+1)	-0.1465875(+1)
D_1 (fm ⁶)	-0.3102824(-1)	-0.1193597(-1)	-0.2144023(-1)
D_2 (fm ⁶)	-0.4438695(-2)	-0.4450346(-2)	0.1386494(-2)
D_3 (fm ⁶)	-0.1351171(-1)	-0.9542801(-2)	-0.1620926(-1)
D_4 (fm ⁶)	-0.7084459(-3)	0.3976205(-2)	0.2071219(-2)
D_5 (fm ⁶)	0.1110108(-1)	0.7809205(-2)	0.7238077(-2)
D_6 (fm ⁶)	-0.8598857(-2)	-0.7362895(-2)	-0.2323562(-2)
D_7 (fm ⁶)	-0.5367908(-1)	-0.4158494(-2)	0.3065351(-1)
D_8 (fm ⁶)	0.3119241(-1)	0.1090986(-1)	0.2957488(-1)
D_9 (fm ⁶)	0.3281636(-1)	0.6095858(-3)	0.9135194(-1)
D_{10} (fm ⁶)	-0.8647128(-1)	-0.5432144(-1)	-0.1196465
D_{11} (fm ⁶)	-0.1167788(-1)	-0.5186422(-2)	-0.3065569(-1)
C_0^{IV} (fm ²)	0.9575695(-2)	0.1077541(-1)	0.1312712(-1)
C_0^{IT} (fm ²)	0.2194758(-1)	0.2102140(-1)	0.1394723(-1)
C_1^{IT} (fm ⁴)	-0.1550501(-2)	0.1152693(-3)	-0.8965197(-2)
C_2^{IT} (fm ⁴)	-0.8354679(-2)	-0.1391786(-2)	-0.3079018(-2)
C_3^{IT} (fm ⁴)	-0.6682746(-2)	-0.3194459(-3)	0.3905867(-4)
C_4^{IT} (fm ⁴)	0.1276971(-1)	0.2879873(-2)	0.8844043(-3)

TABLE IV: The singlet and triplet np , and singlet pp and nn , scattering lengths and effective ranges corresponding to the potential models a , b and c (fitted up to 125 MeV lab energy), and \tilde{a} , \tilde{b} , \tilde{c} (fitted up to 200 MeV lab energy). Experimental values are from Refs. [54–58].

	Experiment	Model a	Model b	Model c	Model \tilde{a}	Model \tilde{b}	Model \tilde{c}
$^1a_{pp}$	−7.8063(26) −7.8016(29)	−7.776	−7.774	−7.769	−7.775	−7.770	−7.769
$^1r_{pp}$	2.794(14) 2.773(14)	2.780	2.771	2.754	2.774	2.760	2.753
$^1a_{nn}$	−18.90(40)	−18.896	−18.921	−18.966	−18.904	−19.009	−18.919
$^1r_{nn}$	2.75(11)	2.825	2.815	2.795	2.819	2.801	2.794
$^1a_{np}$	−23.740(20)	−23.722	−23.739	−23.741	−23.758	−23.754	−23.740
$^1r_{np}$	2.77(5)	2.666	2.686	2.684	2.642	2.682	2.683
$^3a_{np}$	5.419(7)	5.424	5.424	5.423	5.399	5.394	5.424
$^3r_{np}$	1.753(8)	1.761	1.760	1.770	1.727	1.720	1.773

TABLE V: Same as in Table IV but for the deuteron static properties; experimental values are from Refs. [59–62].

	Experiment	Model a	Model b	Model c	Model \tilde{a}	Model \tilde{b}	Model \tilde{c}
E_d (MeV)	2.224575(9)	2.224574	2.224573	2.224576	2.224574	2.224568	2.224570
A_S (fm $^{-1/2}$)	0.8846(9)	0.8862	0.8861	0.8874	0.8811	0.8799	0.8877
η	0.0256(4)	0.0249	0.0248	0.0250	0.0247	0.0245	0.0250
r_d (fm)	1.97535(85)	1.968	1.968	1.971	1.956	1.955	1.971
μ_d (μ_0)	0.857406(1)	0.850	0.849	0.850	0.850	0.850	0.849
Q_d (fm 2)	0.2859(3)	0.268	0.267	0.269	0.263	0.256	0.269
P_d (%)		5.24	5.49	5.32	5.22	5.21	5.35

section, we briefly discuss the HH and QMC methods adopted here for the accurate or exact solution of the few-nucleon Schrödinger equation, $H\Psi = E\Psi$, where Ψ is a nuclear wave function with specific spin, parity and isospin. We then present results for the binding energies and rms radii of the $A = 2$ –6 nuclei with a Hamiltonian H including the nonrelativistic

kinetic energy in combination with the two-body potentials v_{12} of Sec. II. In particular for our calculations we use nuclear wave functions corresponding to models a , \tilde{a} and b , \tilde{b} , whose LECs are specified in Tables II and III.

The HH method is used to calculate the ground-state energies of ${}^3\text{H}$ and ${}^4\text{He}$ and these results provide a benchmark for the corresponding QMC calculations. The QMC methods are then applied to compute binding energies and rms radii of the ${}^3\text{He}$ ground state, of the ${}^6\text{Li}$ and ${}^6\text{He}$ ground and excited states.

A. The Hyperspherical Harmonics Method

The HH method uses hyperspherical-harmonics functions as a suitable expansion basis for the wave function of an A -body system. In the specific case of $A=3$ and 4 nuclei, the corresponding ground-state wave functions $\Psi_A^{J^\pi}$ (J^π being the total angular momentum and parity) can be expanded in the following way:

$$\Psi_3^{1/2^+} = \sum_{[K_3]} u_{[K_3]}(\rho_3) \mathcal{B}_{[K_3]}(\Omega_3) , \quad (8)$$

and

$$\Psi_4^{0^+} = \sum_{[K_4]} u_{[K_4]}(\rho_4) \mathcal{B}_{[K_4]}(\Omega_4) . \quad (9)$$

Here $\mathcal{B}_{[K_3]}(\Omega_3)$ and $\mathcal{B}_{[K_4]}(\Omega_4)$ are fully antisymmetrized HH-spin-isospin functions for three and four nucleons characterized by the set of quantum numbers $[K_3] \equiv [n_1, l_1, l_2, L, s, S, t, T]$ and $[K_4] \equiv [n_1, n_2, l_1, l_2, l_3, l', L, s, s', S, t, t', T]$ respectively. The quantum numbers n_i, l_i and l' enter in the construction of the HH vector and are such that the grand angular momenta are $K_3 = 2n_1 + l_1 + l_2$ and $K_4 = 2n_1 + 2n_2 + l_1 + l_2 + l_3$. The orbital angular momenta l_i (and l' for $A=4$) are coupled to give the total orbital angular momentum L . The total spin and isospin of the vector are indicated with S and T , respectively, and s, s', t, t' are intermediate couplings. A detailed description of the HH method with the explicit expression of the HH-spin-isospin functions can be found in Refs. [64–67].

The hyperspherical coordinates (ρ_A, Ω_A) in Eqs. (8) and (9) are given by the hyperradius, $\rho_A^2 = \sum_{i=1}^{A-1} \mathbf{x}_i^2$ expressed in terms of the $A-1$ Jacobi vectors \mathbf{x}_i of the systems, and the hyperangles $\Omega_A = (\hat{\mathbf{x}}_1 \dots \hat{\mathbf{x}}_{A-1}, \alpha_2 \dots \alpha_{A-1})$, with $\hat{\mathbf{x}}_i$ being the unit Jacobi vectors and α_i the hyperangular variables. For $A=3$, $\cos \alpha_2 = x_2/\rho_3$, and for $A=4$ $\cos \alpha_2 = x_2/\sqrt{x_1^2 + x_2^2}$ and $\cos \alpha_3 = x_3/\rho_4$ [67].

In the present application of the HH method, the hyperradial functions are in turn expanded in terms of generalized Laguerre polynomials multiplied by an exponential function

$$u_\mu(\rho_A) = \sum_m C_{m,\mu} \mathcal{L}_m^{(3A-4)}(z) e^{-z/2}, \quad (10)$$

with $z = \beta\rho_A$, β being a nonlinear parameter, and $\mu \equiv [K_A]$. Introducing the above expansion in Eqs. (8) and (9), we can rewrite $\Psi_A^{J^\pi}$ in the compact form

$$\Psi_A^{J^\pi} = \sum_{m,\mu} C_{m,\mu} \Phi_{m,\mu}(\rho_A, \Omega_A), \quad (11)$$

where the (normalized) complete antisymmetric vectors are

$$\Phi_{m,\mu}(\rho_A, \Omega_A) = \mathcal{L}_m^{(3A-4)}(z) e^{-z/2} \mathcal{B}_{[K_A]}(\Omega_A). \quad (12)$$

The ground state energy E is obtained by applying the Rayleigh-Ritz variational principle, which leads to the following eigenvalue-eigenstate problem

$$\sum_{m',\mu'} (H_{m\mu,m'\mu'} - EI_{m\mu,m'\mu'}) = 0 \quad (13)$$

where $H_{m\mu,m'\mu'}$ are the Hamiltonian matrix elements $\langle m\mu|H|m'\mu'\rangle$ and $I_{m\mu,m'\mu'}$ indicates the matrix elements of the identity matrix. The convergence of the energy E in terms of the size of the basis is studied as follows. The HH functions are collected in channels having specific combinations of the HH-spin-isospin quantum numbers. For the three-nucleon system the basis includes all possible combinations of HH functions up to $l_1 + l_2 = 6$ corresponding to 23 angular-spin-isospin channels with isospin components $T = 1/2, 3/2$. For each channel the hyperangular quantum number n_1 and hyperradial quantum number m are increased until convergence is reached at a level of accuracy of the order of a few keV on the sought energy eigenvalue. In the case of $A = 4$ all possible combinations of HH functions up to $l_1 + l_2 + l_3 = 6$ having $T = 0$ are included, while for the wave function components having $T > 0$ HH-spin-isospin states up to $l_1 + l_2 + l_3 = 2$ are considered. This selection corresponds to about 234 angular-spin-isospin channels. For each channel the hyperangular quantum numbers n_1, n_2 and hyperradial quantum number m are increased until convergence is reached at a satisfactory level of accuracy. Detailed studies of the convergence have been done in Ref. [66], showing that with this kind of expansion an accuracy of about 20 keV can be obtained for the ${}^4\text{He}$ ground state energy.

B. Quantum Monte Carlo Methods

Over the last three decades, QMC methods have been successfully used to study the structure and reactions of light nuclei and nucleonic matter starting from phenomenological interactions. The extensive use of these *ab-initio* methods for computing many of the important properties of light nuclei, such as spectra, form factors, radiative and weak transitions, low-energy scattering and electroweak response, has led to a rather large number of references, where detailed descriptions of QMC algorithms, as well as tests of their accuracy, have been described in detail and discussed at length (see, for example, the review article [13] and references therein for a complete overview of the topic). In this section we briefly outline those features of QMC techniques relevant for the implementation of these methods with the present chiral (and local) NN potentials at N3LO.

The QMC calculations proceed in two steps. The first step is the variational Monte Carlo (VMC) calculation, in which trial wave functions are optimized by minimizing the Hamiltonian. The second consists of the Green's function Monte Carlo (GFMC) calculation, in which the exact wave functions of the nuclear Hamiltonian are projected out of these optimized trial wave functions by evolving them in imaginary time.

In VMC calculations, one assumes a suitably parametrized form for the antisymmetric wave function Ψ_T of a given spin, parity and isospin and optimizes the variational parameters by minimizing the energy expectation value, E_T ,

$$E_T = \frac{\langle \Psi_T | H | \Psi_T \rangle}{\langle \Psi_T | \Psi_T \rangle} \geq E_0 , \quad (14)$$

which is evaluated by Metropolis Monte Carlo integration [68]. The lowest value for E_T is then taken as the approximate ground-state energy. Upper bounds to energies of excited states can also be obtained, either from standard VMC calculations if they have different quantum numbers from the ground state, or from small-basis diagonalizations if they have the same quantum numbers.

The “best” variational wave functions Ψ_T for the nuclei studied in the present work have the form [69]

$$|\Psi_T\rangle = S \prod_{i<j}^A (1 + U_{ij}) |\Psi_J\rangle , \quad (15)$$

where S is the symmetrization operator. The Jastrow wave function Ψ_J is fully antisymmetric and has the $(J^\pi; T)$ quantum numbers of the state of interest, while U_{ij} are the

two-body correlation operators. The correlation functions in U_{ij} are obtained by solving two-body Euler-Lagrange equations projected in pair spin S and isospin T channels, and for finite nuclei are required to satisfy suitable boundary conditions [69]. Since the calculations carried out here are with only two-body interactions, three-body correlations induced by three-body interactions are not explicitly accounted for in Ψ_T .

In order to find the optimum Ψ_T , the minimization of the energy expectation value and its associated variance are carried out with respect to the variational parameters. In the case of $A=6$ nuclei, the optimization of the energies is subject to the constraint that the rms radii are close to the GFMC ones obtained with the AV18. This is because the best variational wave functions we have do not make p-shell nuclei stable against breakup into sub-clusters. The search for the best sets of variational parameters is performed by using the optimization tool NLOpt [72], a free open-source library for nonlinear optimization problems.

Given the best set of variational parameters, the trial wave function Ψ_T can then be used as the starting point of a GFMC [70, 71] calculation which projects out of it the exact lowest energy state Ψ_0 with the same quantum numbers. The projection of Ψ_0 is carried out by evolving for long imaginary time $\tau = -it$

$$|\Psi_0\rangle \propto \lim_{\tau \rightarrow \infty} |\Psi(\tau)\rangle = \lim_{\tau \rightarrow \infty} e^{-(H-E_0)\tau} |\Psi_T\rangle, \quad (16)$$

with the obvious initial condition $|\Psi(\tau=0)\rangle = |\Psi_T\rangle$. In practice the imaginary-time evolution operator $\exp[-(H-E_0)\tau]$ is computed for small time steps $\Delta\tau$ with $\tau = n \Delta\tau$, and is carried out with a simplified version H' of the full Hamiltonian H . In the presence of only NN interactions the Hamiltonian H' contains a charge-independent eight-operator projection, $[\mathbf{1}, \boldsymbol{\sigma}_1 \cdot \boldsymbol{\sigma}_2, S_{12}, \mathbf{L} \cdot \mathbf{S}] \otimes [\mathbf{1}, \boldsymbol{\tau}_1 \cdot \boldsymbol{\tau}_2]$, of the full two-body potential, constructed to preserve the potential in all S and P waves as well as the 3D_1 and its coupling to the 3S_1 .

The desired expectation values of ground-state and low-lying excited-state observables are then computed approximately by stochastic integration of “mixed” matrix elements [74]

$$\langle \mathcal{O}(\tau) \rangle_M = \frac{\langle \Psi(\tau) | \mathcal{O} | \Psi_T \rangle}{\langle \Psi(\tau) | \Psi_T \rangle}, \quad (17)$$

where \mathcal{O} is the observable of interest to be evaluated. By writing $\Psi(\tau) = \Psi_T + \delta\Psi(\tau)$ and neglecting terms of order $[\delta\Psi(\tau)]^2$, one obtains an approximate expression for

$$\langle \mathcal{O}(\tau) \rangle \equiv \frac{\langle \Psi(\tau) | \mathcal{O} | \Psi(\tau) \rangle}{\langle \Psi(\tau) | \Psi(\tau) \rangle} \approx \langle \mathcal{O}(\tau) \rangle_M + [\langle \mathcal{O}(\tau) \rangle_M - \langle \mathcal{O} \rangle_V], \quad (18)$$

where $\langle \mathcal{O} \rangle_V$ is the variational expectation value.

In the case of the Hamiltonian, since the propagator commutes with it, the mixed estimate $\langle H(\tau) \rangle_M$ of Eq. (17) is itself an upper bound to the the ground-state energy E_0 and can be expressed as [74]

$$E(\tau) = \langle H(\tau) \rangle_M = \frac{\langle \Psi(\tau/2) | H | \Psi(\tau/2) \rangle}{\langle \Psi(\tau/2) | \Psi(\tau/2) \rangle}. \quad (19)$$

Because the simpler H' is used to generate the GFMC propagator the total energy is then computed by the mixed estimate of H' plus the difference $\langle H - H' \rangle_M$ evaluated by Eq. (18).

Apart from the use of mixed estimates and H' in the propagation, another source of systematic errors that affects GFMC calculations is the well-known fermion sign problem. In essence this results from the fact that during the imaginary-time propagation bosonic noise gets mixed into the propagated wave function. This bosonic component has a much lower energy than the fermion component and thus is exponentially amplified in subsequent iterations of the short-time propagators. The desired fermionic component is projected out by the antisymmetric Ψ_T when Eq. (17) is evaluated; however, the presence of large statistical errors which increase with τ effectively limits the maximum τ that can be used in the calculations. Since the number of pairs to be exchanged grows with the mass number A , the sign problem also grows exponentially with increasing A .

For spin- and isospin-dependent wave functions, the fermion sign problem can be controlled by a suitable constrained path approximation, which basically limits the initial propagation to regions where the propagated $|\Psi(\tau)\rangle$ and trial $|\Psi_T\rangle$ wave functions have a positive overlap and discards those configurations that instead have a small or vanishing overlap (see Ref. [75] for details on this topic). To address the possible bias that the constrained path technique can introduce in the calculations, all the configurations (also those that would be rejected) for a small number of unconstrained time steps n_{uc} are used when evaluating the expectation values. In general the number n_{uc} is chosen to be as large as possible within a reasonable statistical error.

For phenomenological nuclear Hamiltonians (such those based on the AV18 potential) the constrained-path approximation was not necessary for calculations of $A \leq 4$ systems, since the sign problem was quite mild for these light nuclei. On the other hand, it is essential for GFMC calculations with the N3LO NN chiral interactions of Sec. II, since the sign problem is far more severe for this category of potentials.

C. Results for binding energies

In this section we present results for ground and excited states of ${}^3\text{H}$, ${}^3\text{He}$, ${}^4\text{He}$, ${}^6\text{He}$, and ${}^6\text{Li}$ nuclei using a subset of the local chiral potentials discussed in Sec. II. In particular, in order to solve the ${}^3\text{H}$ and ${}^4\text{He}$ ground states, we use VMC, GFMC, and HH methods with N3LO NN models a , \tilde{a} , b and \tilde{b} , while for ${}^3\text{He}$, ${}^6\text{He}$, and ${}^6\text{Li}$ ground and excited states we present VMC and GFMC calculations performed with model \tilde{b} only.

The variational wave functions used for the VMC results include only spatial and spin-isospin two-body correlations denoted by U_{ij} as in Refs. [69, 74]; the Jastrow wave functions for the s-shell ($A=3$ and 4) and p-shell ($A=6$) nuclei are also given explicitly in those references. For these calculations, the search in parameter space is made using COBYLA (Constrained Optimization BY Linear Approximations) algorithm available in the NLOpt [72] library. The optimal parameters are found typically using runs of 100,000 configurations for the evaluation of matrix elements in Eq. (14). When the optimal trial wave function is found, a long run with 1,000,000, 500,000, and 200,000 configurations is made in $A=3$, 4 and 6 nuclei, respectively, which then is used as input for the GFMC calculations. The GFMC results are obtained using the constrained path technique with $n_{\text{uc}}=20$ unconstrained time steps. The imaginary-time evolution for the a and \tilde{b} models (\tilde{a} and b ones) is computed with small time step $\Delta\tau=0.0005$ (0.0001) MeV^{-1} up to total time $\tau=0.2$ MeV^{-1} .

The results for the ${}^3\text{H}$ and ${}^4\text{He}$ ground states are shown in Tables VI and VII, respectively. The VMC calculations give energies that are 3–4% above the corresponding HH or GFMC predictions; the latter are in good agreement with each other. The errors quoted for the VMC and GFMC results are the Monte Carlo statistical errors. We see that increasing the laboratory energy range, in which the LECs are fitted, from 125 to 200 MeV (as discussed in Sec. III), leads to more binding for these systems.

In Table VIII we report VMC and GFMC calculations for ${}^3\text{H}$, ${}^3\text{He}$, ${}^4\text{He}$, ${}^6\text{He}$, and ${}^6\text{Li}$ ground and excited states obtained using model \tilde{b} , which has, among the N3LO local potentials presented in Sec. II, the “best” behavior in terms of sign problem. In that table we also report the corresponding GFMC calculation obtained with the AV18. We note that for $A=3$, 4 and 6 the binding energies obtained using model \tilde{b} differ by about 0.2–0.3 MeV, 1.07 MeV, and 1.3–0.5 MeV, respectively, from the corresponding ones obtained using AV18.

	Model a		Model \tilde{a}		Model b		Model \tilde{b}	
Method	E_0	$\sqrt{\langle r_p^2 \rangle}$	E_0	$\sqrt{\langle r_p^2 \rangle}$	E_0	$\sqrt{\langle r_p^2 \rangle}$	E_0	$\sqrt{\langle r_p^2 \rangle}$
VMC	-7.592(6)	1.65	-7.691(6)	1.62	-7.317(7)	1.68	-7.643(5)	1.63
GFMC	-7.818(8)	1.62	-7.917(10)	1.60	-7.627(17)	1.65	-7.863(8)	1.57
HH	-7.818		-7.949		-7.599		-7.866	

TABLE VI: The ${}^3\text{H}$ ground-state energies E_0 (MeV) and rms proton radii r_p (fm) with models a , \tilde{a} , b , and \tilde{b} . Statistical errors on the energy evaluations are indicated in parentheses for the VMC and GFMC calculations.

	Model a		Model \tilde{a}		Model b		Model \tilde{b}	
Method	E_0	$\sqrt{\langle r_p^2 \rangle}$	E_0	$\sqrt{\langle r_p^2 \rangle}$	E_0	$\sqrt{\langle r_p^2 \rangle}$	E_0	$\sqrt{\langle r_p^2 \rangle}$
VMC	-24.38(1)	1.51	-25.03(1)	1.49	-22.89(2)	1.54	-24.46(2)	1.49
GFMC	-25.13(5)	1.49	-25.71(3)	1.50	-23.88(5)	1.53	-25.21(4)	1.45
HH	-25.15		-25.80		-23.96		-25.28	

TABLE VII: Same as in Table VI but for the ${}^4\text{He}$ ground state.

The optimization of the ${}^3\text{He}$ ground state has been performed using as starting point the variational parameters for ${}^3\text{H}$, but varying only the separation energies and tensor/central ratios—these parameters characterize the asymptotic boundary conditions imposed on the pair-correlation functions [69]. The calculated VMC energy, as shown in Table VIII, is ~ 0.2 MeV above the GFMC one.

The ground state of ${}^6\text{He}$, not bound with respect to the ${}^4\text{He}$ threshold, is a $(J^\pi, T) = (0^+; 1)$ state which has predominantly a ${}^{2S+1}L[n] = {}^1\text{S}[2]$ character (we use spectroscopic notation to denote the orbital angular momentum L , the spin S and the Young diagram spatial symmetry $[n]$ of the state). The $(2^+; 1)$ first excited state, mostly a ${}^1\text{D}[2]$ state, is above the threshold for decay to $\alpha + 2n$ with a width of ≈ 100 keV and we treat it as a stable state. For both states we allow a possible ${}^3\text{P}[11]$ admixture in the total wave function, and then use generalized eigenvalue routines to diagonalize the resulting 2×2 matrix for each of them and extract the corresponding contributions, ${}^1\text{S}[2]$ and ${}^3\text{P}[11]$ for the $(0^+; 1)$ ground state, and ${}^1\text{D}[2]$ and ${}^3\text{P}[11]$ for the $(2^+; 1)$ excited state. We do not report

the calculated energies for the three ${}^3\text{P}[11]$ states with $(J^\pi, T) = (2^+; 1)$, $(1^+; 1)$, and $(0^+; 1)$ since they have yet to be identified experimentally.

The p -shell spectrum for ${}^6\text{Li}$ consists of a $(1^+; 0)$ ground state which is mostly a ${}^3\text{S}[2]$ state, a triplet of ${}^3\text{D}[2]$ excited states with $(3^+; 0)$, $(2^+; 0)$, and $(1^+; 0)$ components, and a singlet of ${}^1\text{P}[11]$ excited state with a $(1^+; 0)$ component, the latter not yet identified experimentally. The ${}^6\text{Li}$ ground state is stable while the excited states are above the $\alpha + d$ threshold, but we will treat them as bound states below. In addition there are $(0^+; 1)$ and $(2^+; 1)$ excited states that are the isobaric analogs of the ${}^6\text{He}$ states, but they will not be discussed here. For the $(1^+; 0)$ ground and excited states we allow admixtures of ${}^3\text{S}[2]$, ${}^3\text{D}[2]$ and ${}^1\text{P}[11]$ components in the total wave function and then diagonalize a 3×3 matrix to extract the corresponding contributions. This diagonalization procedure is not necessary for the $(3^+; 0)$ and $(2^+; 0)$ excited states since both of them are pure ${}^3\text{D}[2]$ states. The energies of the ${}^3\text{D}[2]$ triplet give a measure of the effective one-body spin-orbit splitting. The J -averaged centroids for both model \tilde{b} and AV18 are 3.6 MeV above their respective ground states; however the spread between lowest and highest triplet members is 1.5 MeV for model \tilde{b} and 2.1 MeV for AV18.

The minimization of the energy for the ${}^6\text{Li}$ ground state has been carried out by requiring the resulting proton rms radius, r_p , to be close to the GFMC one obtained with the AV18. For the excited states, we minimize their energies by requiring that these excited states have radii larger than the ground state. A similar optimization strategy has been adopted for the ${}^6\text{He}$ ground and excited states, except that we use as starting point the ${}^6\text{Li}$ variational parameters and vary only those parameters associated with the single-particle radial functions, ϕ_p , in the Jastrow part of the trial wave function [74].

V. SUMMARY AND CONCLUSIONS

In the present work we have constructed two classes of chiral potentials at N3LO, which are fully local in configuration space, for use (primarily) with HH and QMC methods. The two classes only differ in the range of lab energies over which the LECs in the contact interactions have been fitted to the NN database (as assembled by the Granada group), either 0–125 MeV (models a , b , and c) with $\chi^2/\text{datum} \lesssim 1.1$ for a total of about 2700 data points or 0–200 MeV (models \tilde{a} , \tilde{b} , and \tilde{c}) with $\chi^2/\text{datum} \lesssim 1.4$ for about 3700 data points

TABLE VIII: The ${}^3\text{H}$, ${}^3\text{He}$, ${}^4\text{He}$, ${}^6\text{He}$, and ${}^6\text{Li}$ ground- and excited-state energies in MeV and proton rms radii r_p in fm with model \tilde{b} compared with the corresponding GFMC results obtained with the AV18. Statistical errors on the energy evaluations are indicated in parentheses.

${}^AZ(J^\pi; T)$	VMC		GFMC		GFMC(AV18)	
	E_0	$\sqrt{\langle r_p^2 \rangle}$	E_0	$\sqrt{\langle r_p^2 \rangle}$	E_0	$\sqrt{\langle r_p^2 \rangle}$
${}^3\text{H}(\frac{1}{2}^+; \frac{1}{2})$	-7.643(5)	1.63	-7.863(8)	1.57	-7.610(5)	1.66
${}^3\text{He}(\frac{1}{2}^+; \frac{1}{2})$	-6.907(5)	1.84	-7.115(9)	1.84	-6.880(5)	1.85
${}^4\text{He}(0^+; 0)$	-24.46(2)	1.49	-25.21(4)	1.45	-24.14(1)	1.49
${}^6\text{He}(0^+; 1)$	-22.58(3)	2.05	-24.53(6)	2.07(1)	-23.76(9)	2.06(1)
${}^6\text{He}(2^+; 1)$	-20.94(2)	2.06	-22.87(6)	2.18(2)	-21.85(9)	2.11(1)
${}^6\text{Li}(1^+; 0)$	-25.86(3)	2.58	-27.71(8)	2.62(1)	-26.87(9)	2.58(1)
${}^6\text{Li}(3^+; 0)$	-22.73(3)	2.59	-24.56(8)	2.59(1)	-24.11(7)	2.87(1)
${}^6\text{Li}(2^+; 0)$	-21.42(3)	2.61	-24.04(9)	2.79(2)	-22.75(11)	2.63(1)
${}^6\text{Li}(1\frac{1}{2}^+; 0)$	-20.42(3)	2.58	-23.09(11)	2.89(2)	-21.99(12)	2.85(3)

(representing an increase of roughly 40% in the size of the fitted database relative to the 0–125 MeV case). Within a given class, models a , b , and c (or \tilde{a} , \tilde{b} , and \tilde{c}) have different short-range and long-range cutoff radii, respectively R_L and R_S : $(R_L, R_S) = (1.2, 0.8)$ fm for models a and \tilde{a} , $(1.0, 0.7)$ fm for models b and \tilde{b} , and $(0.8, 0.6)$ fm for models c and \tilde{c} . The cutoff radius R_L regularizes the long-range part of the potential, which includes OPE and TPE terms without and with excitation of intermediate Δ isobars. The cutoff radius R_S provides a range to the δ -functions and their derivatives, which characterize the contact interactions in the short-range part of the potential. These contact interactions require a total of 26 independent LECs, 20 of which occur in the charge-independent (CI) component and 6 in the charge-dependent (CD) one (5 for central, tensor and spin-orbit CIB terms, and 1 for a central CSB term). These 26 LECs are then constrained by the fits above (their values are listed in Tables II and III).

A subset of the potentials— a , \tilde{a} , b , and \tilde{b} —have been used in HH, VMC, and GFMC calculations of binding energies and proton rms radii of nuclei with $A = 2$ –6. The GFMC calculations are rather challenging owing to the serious fermion-sign problem associated with these potentials, even for s-shell nuclei (${}^3\text{H}$, ${}^3\text{He}$, and ${}^4\text{He}$) (this problem becomes

especially severe for models c and \tilde{c} , and they have not been used in the present work). However, implementation of the constrained-path algorithm in the course of the imaginary-time propagation substantially reduces the statistical fluctuations in the energy evaluation, and leads to ${}^3\text{H}$ and ${}^3\text{He}$ ground-state energies in excellent agreement with those obtained in the HH calculations. All present models, especially c and \tilde{c} , have rather strong spin-orbit, quadratic orbital angular momentum, and quadratic spin-orbit components, particularly in the $(S, T) = (1, 0)$ channel: for internucleon separation close to zero, they have values of ~ 2800 MeV, ~ 200 MeV, and ~ 460 MeV respectively, in this channel. While these components vanish for nucleon pairs in relative S-wave, they do so, in the course of a GFMC imaginary-time propagation, only by averaging large values of opposite signs, thus producing large fluctuations.

The models \tilde{a} and \tilde{b} produce more binding in $A = 3$ and 4 nuclei than a and b ; the extra binding of model \tilde{b} relative to b amounts to 5% in ${}^4\text{He}$. It appears that model \tilde{b} leads to ground- and excited-state energies of $A = 3$ –6 nuclei, which are close to those calculated with AV18. Clearly, the next stage in the program of studies of light nuclei structure with chiral interactions we envision, is the inclusion of a three-nucleon potential. A chiral version of it at leading order, including Δ -isobar intermediate states, has been developed, and is currently being constrained by reproducing observables in the $A = 3$ systems.

Acknowledgments

Conversations and e-mail exchanges with J. Carlson and S. Gandolfi are gratefully acknowledged. The work of M.P., A.L., S.C.P., and R.B.W has been supported by the Nuclear Computational Low-Energy Initiative (NUCLEI) SciDAC project. This research is supported by the U.S. Department of Energy, Office of Science, Office of Nuclear Physics, under contracts DE-AC02-06CH11357 (M.P., A.L., S.C.P., and R.B.W.) and DE-AC05-06OR23177 (R.S.). This research also used resources provided by Argonne’s Laboratory Computing Resource Center and by the National Energy Research Scientific Computing

Center (NERSC).

- [1] B.R. Barrett, P. Navrtil, and J.P. Vary, *Progress in Particle and Nuclear Physics* **69** (0), 131 (2013).
- [2] E.D. Jurgenson, P. Maris, R.J. Furnstahl, P. Navrtil, W.E. Ormand, and J.P. Vary, *Phys. Rev. C* **87**, 054312 (2013).
- [3] G. Hagen, T. Papenbrock, A. Ekström, K.A. Wendt, G. Baardsen, S. Gandolfi, M. Hjorth-Jensen, and C.J. Horowitz, *Phys. Rev. C* **89**, 014319 (2014).
- [4] G. Hagen, T. Papenbrock, M. Hjorth-Jensen, and D.J. Dean, *Reports on Progress in Physics* **77** (9), 096302 (2014).
- [5] M. Viviani, L.E. Marcucci, S. Rosati, A. Kievsky, and L. Girlanda, *Few-Body Syst.* **39**, 159 (2006).
- [6] L.E. Marcucci, A. Kievsky, L. Girlanda, S. Rosati, and M. Viviani, *Phys. Rev. C* **80**, 034003 (2009).
- [7] M. Viviani, A. Kievsky, L. Girlanda, L.E. Marcucci, and S. Rosati, *Few-Body Syst.* **45**, 119 (2009).
- [8] M. Viviani, L. Girlanda, A. Kievsky, L.E. Marcucci, and S. Rosati, *EPJ Web Conf.* **3**, 05011 (2010).
- [9] S. Bogner, R. Furnstahl, and A. Schwenk, *Progress in Particle and Nuclear Physics* **65** (1), 94 (2010).
- [10] H. Hergert, S.K. Bogner, S. Binder, A. Calci, J. Langhammer, R. Roth, and A. Schwenk, *Phys. Rev. C* **87**, 034307 (2013).
- [11] W. Dickhoff, and C. Barbieri, *Progress in Particle and Nuclear Physics* **52** (2), 377 (2004).
- [12] V. Somà, C. Barbieri, and T. Duguet, *Phys. Rev. C* **87**, 011303 (2013).
- [13] J. Carlson *et al.*, *Rev. Mod. Phys.* **87**, 1067 (2015).
- [14] S. Weinberg, *Phys. Lett.* **B251**, 288 (1990); *Nucl. Phys.* **B363**, 3 (1991); *Phys. Lett.* **B295**, 114 (1992).
- [15] E. Epelbaum, H. W. Hammer, and U.-G. Meißner, *Rev. Mod. Phys.* **81**, 1773 (2009).
- [16] R. Machleidt and D.R. Entem, *Phys. Rep.* **503**, 1 (2011).
- [17] N. Kalantar-Nayestanaki *et al.*, *Rept. Prog. Phys.* **75**, 016301 (2012).

- [18] H. W. Hammer, A. Nogga, and A. Schwenk, *Rev. Mod. Phys.* **85**, 197 (2013).
- [19] N. Kaiser, R. Brockmann, and W. Weise, *Nucl. Phys. A* **625**, 758 (1997).
- [20] N. Kaiser, S. Gerstendörfer, and W. Weise, *Nucl. Phys. A* **637**, 395 (1998).
- [21] N. Kaiser, *Phys. Rev. C* **61**, 014003 (1999).
- [22] N. Kaiser, *Phys. Rev. C* **62**, 024001 (2000).
- [23] N. Kaiser, *Phys. Rev. C* **63**, 044010 (2001).
- [24] N. Kaiser, *Phys. Rev. C* **64**, 057001 (2001).
- [25] N. Kaiser, *Phys. Rev. C* **65**, 017001 (2002).
- [26] E. Epelbaum, W. Glöckle, and U.-G. Meißner, *Nucl. Phys. A* **637**, 107 (1998); *A* **671**, 295 (2000).
- [27] D.R. Entem and R. Machleidt, *Phys. Rev. C* **66**, 014002 (2002).
- [28] H. Krebs, E. Epelbaum, and Ulf.-G. Meißner, *Eur. Phys. J. A* **32**, 127 (2007).
- [29] D.R. Entem and R. Machleidt, *Phys. Rev. C* **68**, 041001(R) (2003).
- [30] E. Epelbaum, W. Glöckle, and U.-G. Meißner, *Nucl. Phys. A* **747**, 362 (2005).
- [31] D. Siemens, V. Bernard, E. Epelbaum, A. Gasparyan, H. Krebs, Ulf-G. Meißner, [arXiv:1602.02640\[nucl-th\]](https://arxiv.org/abs/1602.02640) (2016).
- [32] De-Liang Yao, D. Siemens, V. Bernard, E. Epelbaum, A.M. Gasparyan, J. Gegelia, H. Krebs, Ulf-G. Meißner, [arXiv:1603.03638\[nucl-th\]](https://arxiv.org/abs/1603.03638) (2016).
- [33] D.R. Entem, N. Kaiser, R. Machleidt, and Y. Nosyk, *Phys. Rev. C* **91**, 014002 (2015).
- [34] E. Epelbaum, H. Krebs, U.-G. Meißner, *Phys. Rev. Lett.* **115**, 122301 (2015).
- [35] D.R. Entem, N. Kaiser, R. Machleidt, and Y. Nosyk, *Phys. Rev. C* **92**, 064001 (2015).
- [36] V.G.J. Stoks, R.A.M. Klomp, M.C.M. Rentmeester, and J.J. de Swart, *Phys. Rev. C* **48**, 792 (1993).
- [37] V.G.J. Stoks, R.A.M. Klomp, C.P.F. Terheggen, and J.J. de Swart, *Phys. Rev. C* **49**, 2950 (1994).
- [38] R.A. Arndt, I.I. Strakovsky, and R.L. Workman, SAID, Scattering Analysis Interactive Dial-in computer facility, George Washington University (formerly Virginia Polytechnic Institute), solution SM99 (Summer 1999).
- [39] R. Navarro Pérez, J.E. Amaro, and E. Ruiz Arriola, *Phys. Rev. C* **88**, 064002 (2013); *Phys. Rev. C* **89**, 024004 (2014); *Phys. Rev. C* **89**, 064006 (2014).
- [40] A. Ekström, G.R. Jansen, K.A. Wendt, G. Hagen, T. Papenbrock, B.D. Carlsson, C. Forssén,

- M. Hjorth-Jensen, P. Navrátil, and W. Nazarewicz, Phys. Rev. C **91**, 051301(R) (2015).
- [41] R. B. Wiringa, V. G. J. Stoks, and R. Schiavilla, Phys. Rev. C **51**, 38 (1995).
- [42] J. Carlson, V.R. Pandharipande, and R.B. Wiringa, Nucl. Phys. A **401**, 59 (1983).
- [43] B.S. Pudliner, A. Smerzi, J. Carlson, V.R. Pandharipande, Steven C. Pieper, and D.G. Ravenhall, Phys. Rev. Lett. **76**, 2416 (1996).
- [44] S.C. Pieper, AIP Conf. Proc. **1011**, 143 (2008).
- [45] S.C. Pieper, V.R. Pandharipande, R.B. Wiringa, and J. Carlson, Phys. Rev. C **64**, 014001 (2001).
- [46] A. Gezerlis *et al.*, Phys. Rev. Lett. **111** (3), 032501 (2013).
- [47] A. Gezerlis, I. Tews, E. Epelbaum, M. Freunek, S. Gandolfi, K. Hebeler, A. Nogga, and A. Schwenk, Phys. Rev. C **90**, 054323 (2014).
- [48] J.E. Lynn, J. Carlson, E. Epelbaum, S. Gandolfi, A. Gezerlis, and A. Schwenk, Phys. Rev. Lett. **113**, 192501 (2014).
- [49] J.E. Lynn, I. Tews, J. Carlson, S. Gandolfi, A. Gezerlis, K.E. Schmidt, and A. Schwenk, Phys. Rev. Lett. **116**, 062501 (2016).
- [50] M. Piarulli, L. Girlanda, R. Schiavilla, R. Navarro Pérez, J.E. Amaro, and E. Ruiz Arriola, Phys. Rev. C **91**, 024003 (2015).
- [51] B. Long and V. Lensky, Phys. Rev. C **83**, 045206 (2011).
- [52] M. Kortelainen, T. Lesinski, J. Moré, W. Nazarewicz, J. Sarich, N. Schunck, M.V. Stoitsov, and S. Wild, Phys. Rev. C **82**, 024313 (2010).
- [53] F.L. Gross and A. Stadler, Phys. Rev. C **78**, 014005 (2008).
- [54] J. R. Bergervoet, P. C. van Campen, W. A. van der Sanden, and J. J. de Swart, Phys. Rev. C **38** (1988) 15.
- [55] W. A. van der Sanden, A. H. Emmen, and J. J. de Swart, Report No. THEF-NYM-83.11, Nijmegen (1983), unpublished; quoted in [54].
- [56] Q. Chen *et al.*, Phys. Rev. C **77** (2008) 054002.
- [57] G. A. Miller, M. K. Nefkens, and I. Slaus, Phys. Rep. **194** (1990) 1.
- [58] R. Machleidt, Phys. Rev. C **63** (2001) 024001.
- [59] T. E. O. Ericson and M. Rosa-Clot, Nucl. Phys. A **405**, 497 (1983).
- [60] N. L. Rodning and L. D. Knutson, Phys. Rev. C **41**, 898 (1990).
- [61] A. Huber, T. Udem, B. Gross, J. Reichert, M. Kouroggi, K. Pachucki, M. Weitz and T. W.

- Hansch, Phys. Rev. Lett. **80**, 468 (1998).
- [62] J. Martorell, D. W. L. Sprung and D. C. Zheng, Phys. Rev. C **51**, 1127 (1995).
- [63] M. Piarulli, L. Girlanda, L.E. Marcucci, S. Pastore, R. Schiavilla, and M. Viviani, Phys. Rev. C **87**, 014006 (2013).
- [64] A. Kievsky, M. Viviani, and S. Rosati, Nucl. Phys. A **577**, 511 (1994).
- [65] A. Kievsky, L.E. Marcucci, S. Rosati, and M. Viviani, Few-Body Syst. **22**, 1 (1997).
- [66] M. Viviani, A. Kievsky, and S. Rosati, Phys. Rev. C **71**, 024006 (2005).
- [67] A. Kievsky, S. Rosati, M. Viviani, L.E. Marcucci, and L. Girlanda, J. Phys. G: Nucl. Part. Phys. **35**, 063101 (2008).
- [68] N. Metropolis, A. W. Rosenbluth, M. N. Rosenbluth, A. H. Teller, and E. Teller, J. Chem. Phys. **21**, 1087 (1953).
- [69] R.B. Wiringa, Phys. Rev. C **43**, 1585 (1991).
- [70] J. Carlson, Phys. Rev. C **36**, 2026 (1987).
- [71] J. Carlson, Phys. Rev. C **38**, 1879 (1988).
- [72] <http://ab-initio.mit.edu/wiki/index.php/NLopt>
- [73] J.E. Lynn and K.E. Schmidt, Phys. Rev. C **86**, 014324 (2012).
- [74] B.S. Pudliner, V.R. Pandharipande, J. Carlson, Steven C. Pieper, and R.B. Wiringa, Phys. Rev. C **56**, 1720 (1997).
- [75] R.B. Wiringa, Steven C. Pieper, J. Carlson, and V.R. Pandharipande, Phys. Rev. C **62**, 014001 (2000).